







**First-principles equation of state of CHON resin for inertial confinement fusion applications**Shuai Zhang <sup>1,\*</sup>, Valentin V. Karasiev,<sup>1</sup> Nathaniel Shaffer <sup>1</sup>, Deyan I. Mihaylov <sup>1</sup>, Katarina Nichols,<sup>1</sup> Reetam Paul,<sup>1</sup> R. M. N. Goshadze,<sup>1</sup> Maitrayee Ghosh <sup>1</sup>, Joshua Hinz,<sup>1</sup> Reuben Epstein <sup>1</sup>, Stefan Goedecker,<sup>2</sup> and S. X. Hu <sup>1,†</sup><sup>1</sup>Laboratory for Laser Energetics, University of Rochester, Rochester, New York 14623, USA<sup>2</sup>Department of Physics, University of Basel, Klingelbergstrasse 82, CH-4056 Basel, Switzerland

(Received 13 July 2022; revised 3 September 2022; accepted 24 September 2022; published 20 October 2022)

A wide-range (0 to 1044.0 g/cm<sup>3</sup> and 0 to 10<sup>9</sup> K) equation-of-state (EOS) table for a CH<sub>1.72</sub>O<sub>0.37</sub>N<sub>0.086</sub> quaternary compound has been constructed based on density-functional theory (DFT) molecular-dynamics (MD) calculations using a combination of Kohn-Sham DFT MD, orbital-free DFT MD, and numerical extrapolation. The first-principles EOS data are compared with predictions of simple models, including the fully ionized ideal gas and the Fermi-degenerate electron gas models, to chart their temperature-density conditions of applicability. The shock Hugoniot, thermodynamic properties, and bulk sound velocities are predicted based on the EOS table and compared to those of C-H compounds. The Hugoniot results show the maximum compression ratio of the C-H-O-N resin is larger than that of CH polystyrene due to the existence of oxygen and nitrogen; while the other properties are similar between CHON and CH. Radiation hydrodynamic simulations have been performed using the table for inertial confinement fusion targets with a CHON ablator and compared with a similar design with CH. The simulations show CHON outperforms CH as the ablator for laser-direct-drive target designs.

DOI: [10.1103/PhysRevE.106.045207](https://doi.org/10.1103/PhysRevE.106.045207)**I. INTRODUCTION**

Laser-direct-drive (LDD) [1] and indirect-drive [2] targets in inertial confinement fusion (ICF) experiments typically consist of a spherical ablator capsule that covers a deuterium-tritium (DT) fuel layer. Polystyrene (CH) has widely been used as the ablator material, which is easy to fabricate and has relatively well-understood equation of state. The disadvantage of CH being susceptible to the Rayleigh-Taylor instability, however, has driven exploration of materials with high tensile strength as alternatives for ablators. Examples include high-density carbon, boron nitride, and boron carbide, which typically exhibit higher ablation pressure and x-ray absorption and can improve the target performance in such experiments. Beside the high-strength materials, other techniques have also been explored. One example is the recently proposed foam layer (through additive manufacture) to mitigate laser imprint and reduce hydrodynamic instabilities during ablation [3], which is an important factor in LDD experiments.

One strategy being explored is to use two-photon polymerization (TPP) to fabricate targets from CHON polyacrylate resin. Using this technique, the CHON material can be precisely fabricated into shell structures with superb lateral structure uniformity (to the level of 1 μm) and radial density gradients (resembling that of bulk resin at the interior and foam at the exterior), which can mitigate the growth rate of Rayleigh-Taylor instability [4]. The fill tube can also be additively manufactured with the capsule as a single component.

High-quality equation of state (EOS) of the target materials are required for designs of ICF and high-energy-density (HED) experiments. However, in contrast to CH, whose EOS has been widely studied experimentally and theoretically [5–14], an EOS for the CHON quaternary compound is still missing. The goal of this work is to provide a first-principles EOS for CHON to be used for hydrodynamic simulations, as well as to benchmark the performance of the new CHON against traditional CH materials. This is important for the design of future ICF and HED experiments that use ablators made of this material.

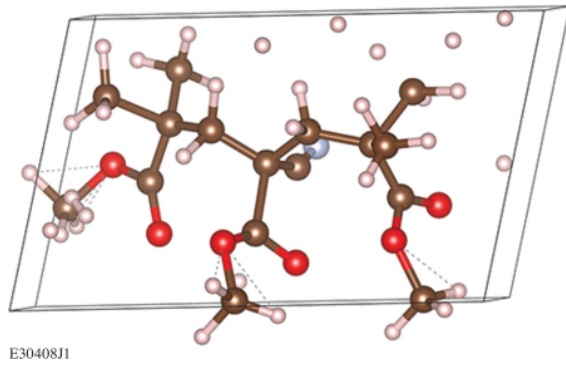
The manuscript is organized as follows: Sec. II introduces the structural preparation and the computational methodology; Sec. III shows the resultant EOS and comparison with other EOS models and pure CH, including the performance based on a preliminary one-dimensional (1D) hydrodynamic simulation; and Sec. IV concludes the paper.

**II. METHODOLOGY****A. Structure preparation**

The CHON resin material used for TPP printing of targets has a bulk density of 1.2 g/cm<sup>3</sup> and empirical formula of CH<sub>1.72</sub>O<sub>0.37</sub>N<sub>0.086</sub> [15]. In this study, we built an atomistic structure model for the CHON resin based on a half of that of polycyanoacrylate [16], where three CN pairs were replaced by CH<sub>3</sub> units and an additional H<sub>2</sub> molecule was introduced to obtain a 50-atom unit cell with 16 C, 27 H, 6 O, and 1 N atom–stoichiometry that matches the resin material in laboratory [17]. The ambient-pressure structure is optimized through full relaxation of the unit cell by Kohn-Sham (KS) density-functional theory (DFT) [18,19] calculations using

\*szha@lle.rochester.edu

†shu@lle.rochester.edu



E30408J1

FIG. 1. A snapshot of the 50-atom CHON unit cell after KS-DFT-MD simulations at  $1.2 \text{ g/cm}^3$  and  $1000 \text{ K}$ , which consists of a C-H-O-N frame and a  $\text{H}_2$  molecule. Edges of the periodic cell are shown with gray lines. Brown, cream, red, and blue spheres represent C, H, O, and N atoms, respectively.

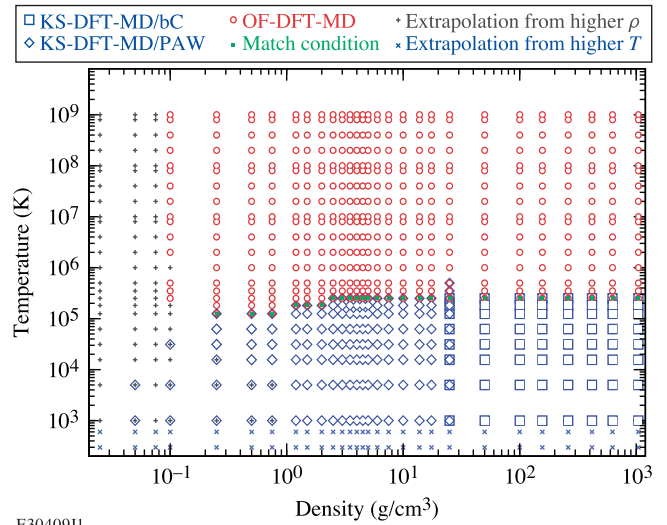
a strongly constrained and appropriately normed (SCAN) exchange-correlation functional [20].

Solid structures for densities higher than ambient are obtained by first shrinking and then partial relaxation (lattice vectors fixed while atoms allowed to move) of the cell. The procedure is performed starting from the ambient structure and gradually increasing density until the system is 20 times denser than the ambient condition. To relax the constraints in cell shape, we have then performed full relaxation at a series of pressures by starting from structures that have been partially relaxed at nearby volumes. Lastly, partial relaxation is performed at each of the target densities by starting from the fully relaxed configuration at a nearby pressure. The resultant structures were used as the starting configuration in our KS-DFT molecular dynamics (KS-DFT-MD) simulations along corresponding isochores.

For lower-than-ambient densities, structures were prepared at  $1000 \text{ K}$  by KS-DFT-MD simulations starting at  $0.75 \text{ g/cm}^3$ ; then the cell was gradually expanded. This procedure retains the basic molecular units in the simulation cell and is continued for a series of densities down to  $0.05 \text{ g/cm}^3$ . The resultant structures were used for higher-temperature KS-DFT-MD simulations along corresponding isochores.

Figure 1 shows a snapshot of the simulation cell after our KS-DFT-MD simulation at  $1.2 \text{ g/cm}^3$  and  $1000 \text{ K}$ , which has a triclinic structure that is similar to the relaxed structures at higher densities. At temperatures above  $15\,000 \text{ K}$  or densities above  $20.0 \text{ g/cm}^3$ , our tests show the cell shape has little effect on the EOS. Therefore we switched to a 50-atom cubic cell at such conditions, except for densities of  $100 \text{ g/cm}^3$  and above, where a 100- to 400-atom cell was used to reduce finite size effects.

We perform first-principles MD calculations of the EOS along 27 isochores (density ranges between  $0.05$  and  $1044.0 \text{ g/cm}^3$ ) at 24 different temperatures (between  $1000$  and  $10^9 \text{ K}$ ). These data have been extrapolated to lower densities and temperatures to produce a wide-range EOS table (shown in Fig. 2). Details of our methodology are presented below.



E30409J1

FIG. 2. Temperature-density grid of the EOS data for CHON produced in this work. The data at densities below  $0.025 \text{ g/cm}^3$  are extrapolated based on the Redlich-Kwong fit of data between  $0.1$  and  $1.0 \text{ g/cm}^3$  and therefore not shown for clarity. “bC”: bare Coulomb.

### B. Kohn-Sham DFT MD for low-temperature calculations

We perform KS-DFT-MD simulations for relatively low-temperature (from  $1000 \text{ K}$  up to  $500\,000 \text{ K}$ ) conditions by using the plane-wave DFT code VASP (Vienna *Ab initio* Simulation Package) [21]. We use the recently developed thermal exchange correlation functional T-SCAN-L, which takes into account electronic thermal and nonhomogeneity effects at the meta-generalized gradient approximation (meta-GGA) level of theory [22], preserving the meta-GGA-level accuracy of SCAN-L [23] at low temperatures—an improvement over previous calculations that typically use GGA or local density approximation functionals. Two types of potentials, projector augmented wave (PAW) [24] and bare-Coulomb [25], have been employed, depending on the density. The PAW potentials (used for simulations up to  $25 \text{ g/cm}^3$ ) explicitly treat the  $1s$  electron of H and all second-shell electrons of C, O, and N as valence, and have  $0.8$  and  $1.1$  Bohr core radii for H and the other elements, respectively. A large energy cutoff of  $2000 \text{ eV}$  is used in the PAW calculations, which is the same as that used in previous work for CH [12,13].

At densities above  $25 \text{ g/cm}^3$ , we have switched to bare-Coulomb potentials to eliminate errors from overlapping of the frozen  $1s$  cores of the PAW potentials. A cutoff energy of  $70\,000 \text{ eV}$  is chosen for the bare-Coulomb calculations. A rigid shift of  $500 \text{ eV/atom}$  was applied to all bare-Coulomb energies to align with those from PAW calculations (see Appendix A 1). The strategy of switching potentials at  $25 \text{ g/cm}^3$  and the validity of using bare-Coulomb at high densities are verified through all-electron calculations using the Quantum Espresso code [26] and a hard set of local pseudopotentials (LPPs), transferable to extreme conditions of high pressure and temperature (see details in Sec. IIC), for selected snapshots (see Appendix A 2). We note that previous studies [27,28] have employed VASP and the bare-Coulomb potentials for calculations of pure C and H at similarly high

densities. To our knowledge, usage of the potentials for O and N or applications to quaternary compounds have not been reported. Due to flexibility of the Quantum Espresso code, we use it and in-house-built all-electron LPP potentials to cross-check the validity of the bare-Coulomb results from VASP. Except for the differences in computational efficiency, DFT implementation in the different codes would perform similarly [29].

In all calculations, the Baldereschi mean-value point [30] is used to sample the Brillouin zone if cubic cells are used, while a  $\Gamma$ -centered  $2 \times 2 \times 2$   $k$  mesh is used for simulations with triclinic cells. The number of orbitals are explicitly set to be large enough to ensure the highest energy state has negligible occupancy (about  $10^{-5}$  or smaller). A Nosé-Hoover thermostat [31,32] is used to generate canonical ensembles at each temperature-density condition of interest, while electrons are enforced to follow a Fermi-Dirac distribution with the temperature equal to that of the ions [33]. A typical KS-DFT-MD trajectory consists of 2000 steps (time step is 0.001 to 0.5 fs). When analyzing the EOS, we discarded the beginning part (typically 20%) of each MD trajectory to ensure that the reported EOS represents that under thermodynamic equilibrium. Ion kinetic contributions to the EOS are manually included by following an ideal gas formula (i.e., internal energy  $E_{\text{ion kin}} = 3Nk_B T/2$  and pressure  $P_{\text{ion kin}} = 3Nk_B T/V$ , where  $k_B$  is the Boltzmann constant,  $N$  denotes the total number of ions in the simulation cell), while all other contributions (ion-ion, ion-electron, and electron-electron interactions and the electron kinetic term) are calculated explicitly.

### C. Orbital-free DFT MD for high-temperature calculations

KS-DFT-MD calculations become increasingly formidable at higher temperatures because of thermal excitation of the electrons to more orbitals at higher energy. We have calculated the CHON EOS at  $10^5$  K or higher temperatures by employing an orbital-free (OF) DFT MD approach with the Luo-Karasiev-Trickey  $\gamma$  Thomas-Fermi (LKT $\gamma$ TF) tunable noninteracting free-energy functionals [34]. The thermal functional is constructed through a convex combination of LKT GGA [35] and TF [36] functionals:

$$\mathcal{F}_s^{\text{LKT}\gamma\text{TF}}[n, T] = \gamma \mathcal{F}_s^{\text{LKT}}[n, T] + (1 - \gamma) \mathcal{F}_s^{\text{TF}}[n, T], \quad (1)$$

where  $\gamma$  is a tuning parameter that varies between 0 and 1, depending on the thermodynamic conditions [34]. This represents another improvement over previous EOS studies that employ the similar strategy of stitching KS and OF but use TF functional in the OF calculations [9,37–39]. In our calculations at  $0.1 \text{ g/cm}^3$ ,  $\gamma$  is fixed to 1.0; for densities of  $0.25 \text{ g/cm}^3$  or higher, we first determine the value of  $\gamma$  for each density by matching the pressure from our OF-MD calculations at a high temperature ( $1$  to  $3 \times 10^5$  K, shown with green squared symbols in Fig. 2) to the corresponding value from our KS-DFT-MD calculations. Then the same  $\gamma$  is applied for all higher-temperature OF-DFT-MD calculations along the corresponding isochore. Finally, the resultant OF-DFT-MD energies along each isochore are shifted to agree with the KS-DFT-MD value at the matching temperature. This procedure ensures that there are no discontinuities in the EOS caused by switching from KS to OF. The values of  $\gamma$  determined

for CHON in this study and the matching conditions are shown in Fig. 15. To ensure thermodynamic consistency, we used the same thermal T-SCAN-L exchange-correlation in OF- as in KS-DFT-MD simulations.

In OF-DFT-MD, we used two sets of LPPs. A hard one (dual-space Gaussian all-electron LPPs [40] for C, H, O, and N) was used for high densities ( $\geq 10 \text{ g/cm}^3$ ) and a softer one (an LPP for H as described in Ref. [41] and all-electron ones for C, O, and N generated using the procedure described in Ref. [42] and presented in the dual-space Gaussian analytic form) for low densities ( $\leq 7.5 \text{ g/cm}^3$ ). The hard pseudopotentials contain only the local part of the dual-space Gaussian pseudopotentials, and are fitted to several strongly excited and ionized configurations of the atoms [43]. Because of the extreme conditions under which these pseudopotentials are used, the excitations and ionizations were chosen to be stronger than for standard pseudopotentials, including energy differences of up to 0.3 Hartree. Accuracy of the soft set of LPPs is verified against the hard ones by comparison between OF-DFT-MD simulations at selected thermodynamic conditions. All OF-DFT-MD simulations were performed with PROFESS@QUANTUM-ESPRESSO package [44] and, depending on the real-space simulation cell size, on a  $128 \times 128 \times 128$  or  $256 \times 256 \times 256$  numerical grid.

### D. Extrapolation to low densities and low temperatures

Accurate DFT-MD simulations at low density become extremely taxing due to the large cell volume and the need for long trajectories. In order to extend the EOS table below  $0.1 \text{ g/cc}$ , we extrapolated each isotherm using analytic fits based on the Redlich-Kwong model [45]. The pressure is fit on each isotherm to

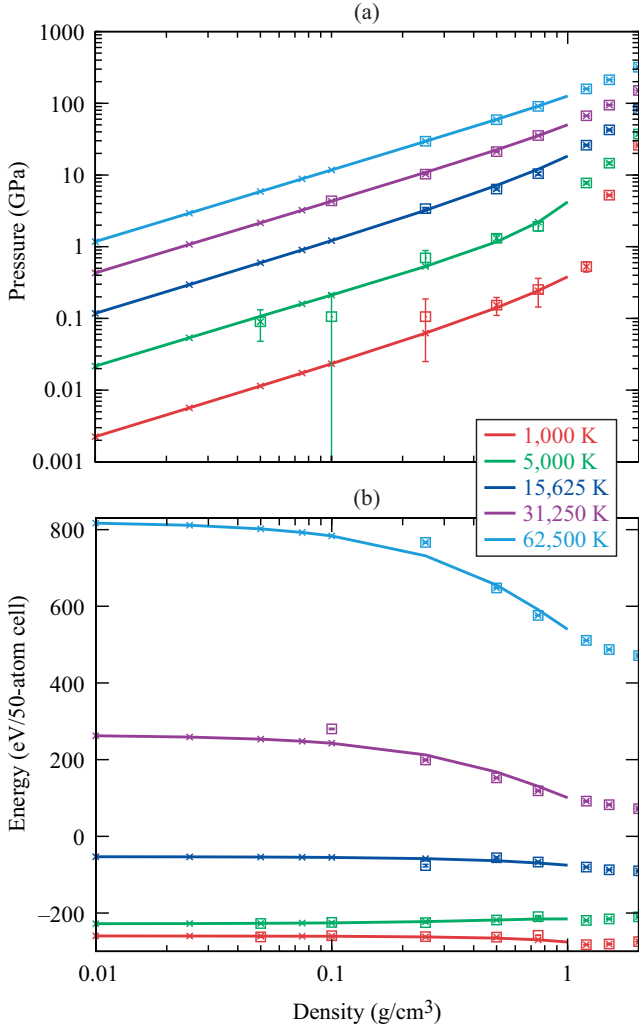
$$P(\rho, T) = \frac{RT}{M_m(T)} \frac{\rho}{1 - B(T)\rho} - \frac{A(T)\rho^2}{1 + B(T)\rho}, \quad (2)$$

where  $R$  is the gas constant, and  $M_m$ ,  $A$ , and  $B$  are fit parameters corresponding to the mean molar mass, attractive coefficient, and molecular covolume. The specific energy is then fit to

$$e(\rho, T) = e_0 + (C_a - 1) \frac{A}{B} \ln(1 - B\rho) - \frac{RT}{M_m} C_m \ln(1 - B\rho) + C_b \left( \frac{A\rho}{1 + B\rho} - \frac{A}{B} \ln(1 + B\rho) - \frac{RT}{M_m} \frac{B\rho}{1 - B\rho} \right) \quad (3)$$

with  $e_0$ ,  $C_a$ ,  $C_b$ , and  $C_m$  as fit parameters. The functions were fitted by using nonlinear least squares with bounds enforced on certain parameters to ensure their values are physically correct (e.g., the molar mass parameter must be positive). Note that because each isotherm is fit independently, thermodynamic consistency is not assured in the low-density portion of the table.

Figure 3 shows the fitting/extrapolation produces pressure and energy isotherms (colored curves) that match the first-principles values but are much smoother and extrapolate to a physically plausible zero-density limit. This provides a useful solution to filling the very low-density regime of the EOS table, which is barely accessible to direct first-principles



E30410J1

FIG. 3. Fit of (a) low-density (up to 1.2 g/cm<sup>3</sup>) pressures and (b) energies data (empty squares) to a Redlich-Kwong model along different isotherms (line-crosses).

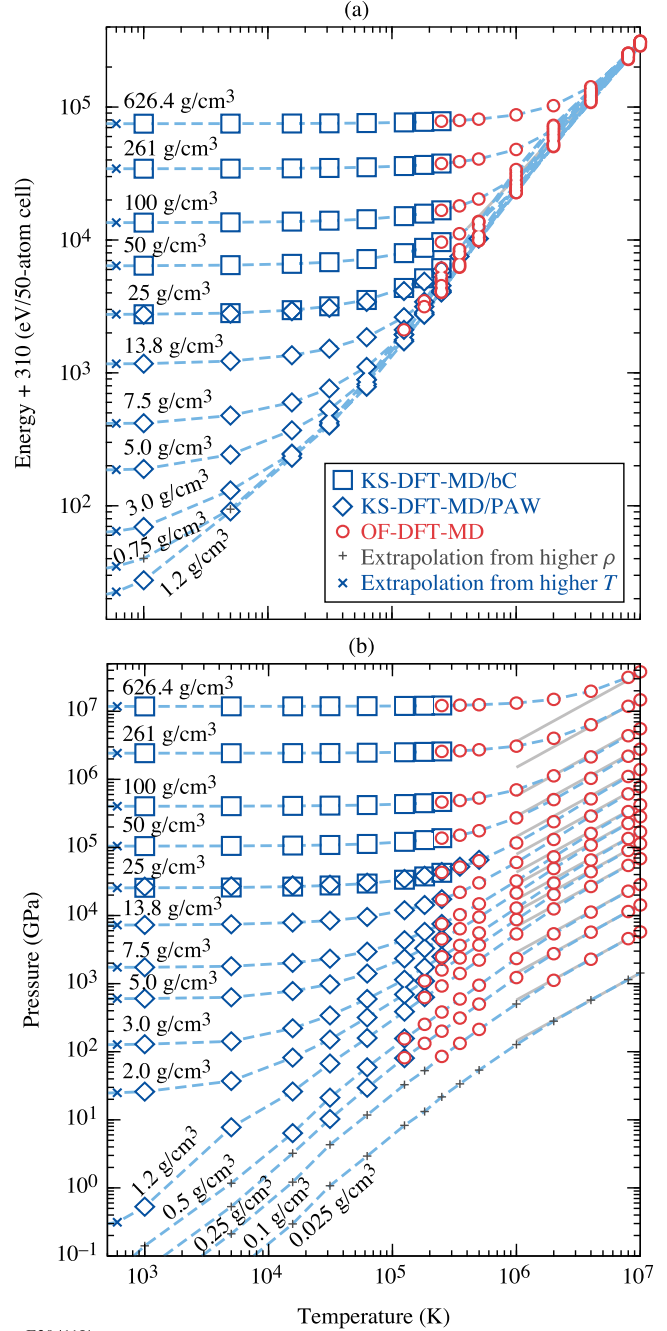
simulations but needed to exist for performing hydrodynamic simulations.

The low-temperature regime is jointly constrained by the cold curve ( $T = 0$  K), calculated using KS-DFT at densities between 1.2 and 17.5 g/cm<sup>3</sup> [46], and the calculated/extrapolated data at  $T \geq 1000$  K. This has been accomplished numerically for each isochore with interpolation (at densities 1.2 to 17.5 g/cm<sup>3</sup>) or extrapolation (at other densities) using cubic splines. We note that this methodology works better at higher-than-ambient than at lower densities, and the uncertainty in the low density, low temperature regime does not affect using this EOS table for typical ICF applications (see Appendix A 4).

### III. RESULTS

#### A. EOS and pair-correlation functions

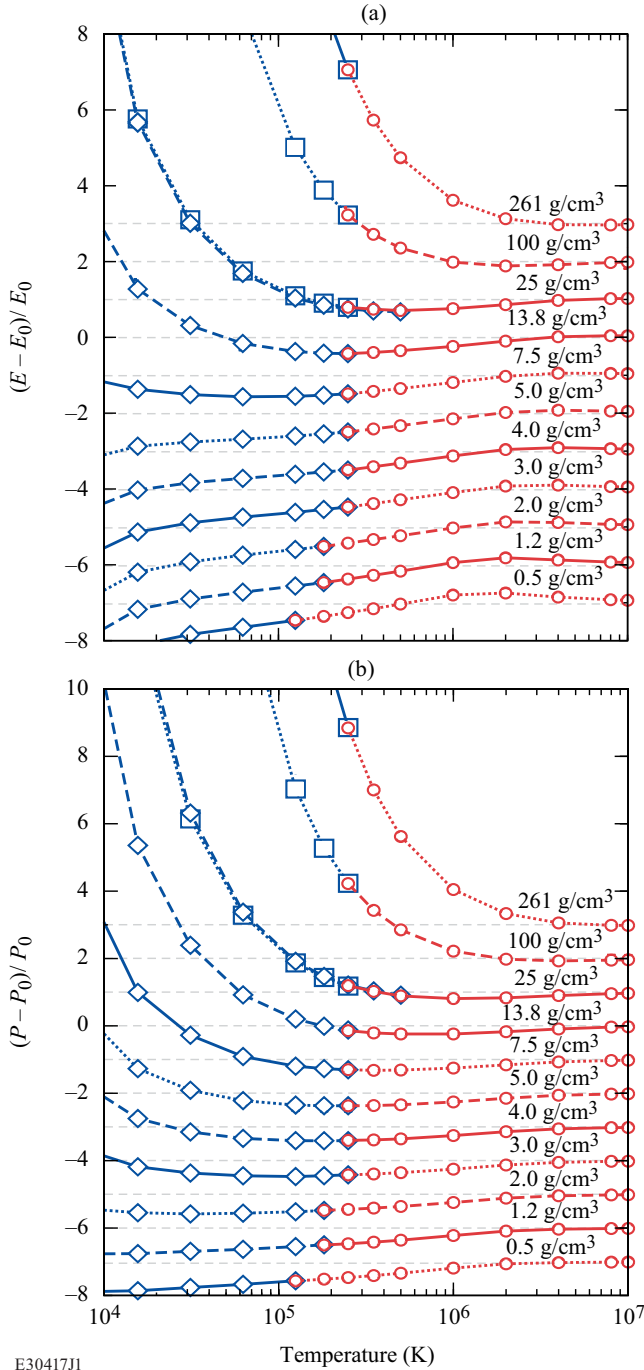
Our calculated EOS at selected densities as functions of temperature is summarized in Fig. 4, which shows good



E30411J1

FIG. 4. (a) Internal energy and (b) pressure of CHON along different isochores considered in this study. “bC”: bare Coulomb. Gray lines denote corresponding values for a fully ionized ideal gas. The energies have been uniformly lifted by 310 eV/50-atom cell to ensure positive values for the logarithmic plot.

agreement between PAW and bare-Coulomb results along the entire 25-g/cm<sup>3</sup> isochore and smooth bridging of KS and OF data at the matching temperatures. Figure 4 also shows monotonic increasing in energy and pressure with temperature due to the increased ion and electron thermal contributions. The variations with temperature become smaller at higher densities because of the increased degeneracy of electrons. The

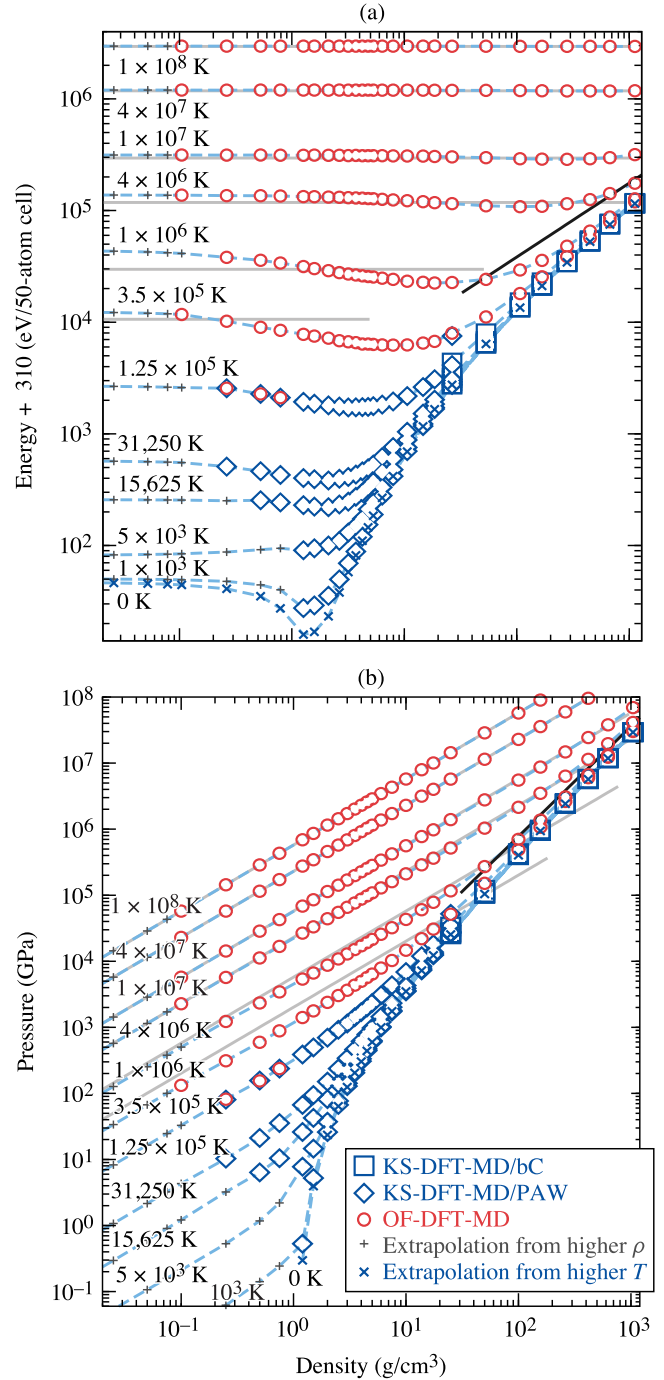


E30417J1

FIG. 5. Matching KS (blue) and OF (red) data in (a) energy and (b) pressure along selected isochores in this work. Data shown are relative to values of fully ionized ideal gas (denoted by  $E_0$  and  $P_0$  and shown with black dotted horizontal lines). Blue diamonds and squares denote calculations using PAW and bare-Coulomb potentials, respectively. Different isochores have been shifted apart for clarity.

EOS approaches that of a fully ionized ideal gas in the limit of high temperatures ( $10^6$  to  $10^7$  K, higher at higher densities).

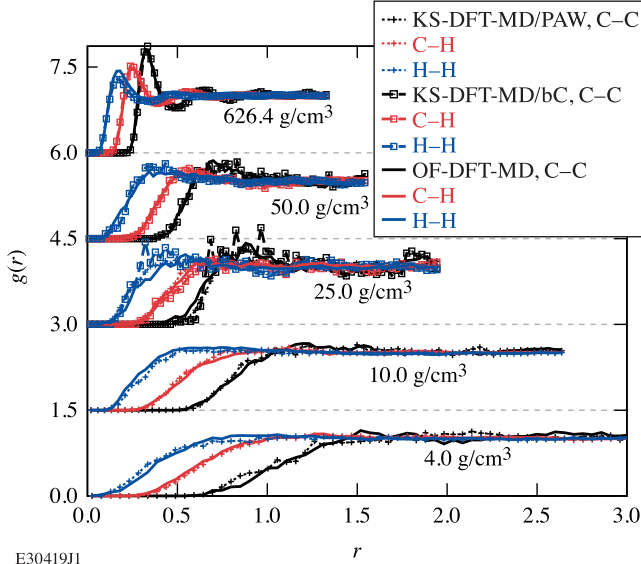
Figure 5 compares the differences between our first-principles EOS and that of a fully ionized ideal gas at selected densities, calculated by  $E_0 = 3N_{n+e}k_B T/2$  and  $P_0 =$



E30418J1

FIG. 6. (a) Internal energy and (b) pressure of CHON along different isotherms considered in this study. “bC”: bare Coulomb. Gray lines represent the fully ionized ideal gas value. Black lines denote the Fermi degenerate electron gas values at zero K.

$N_{n+e}k_B T/V$ , where  $N_{n+e}$  is the total number of particles (nuclei and electrons). Different isochores have been shifted apart, which clearly shows agreements between PAW and bare-Coulomb data. Figure 5 also shows how the EOS data evolve with temperature and the OF-MD data approach that of the fully ionized ideal gas in energy and in pressure. The slope variations in the energy plots between different densities re-



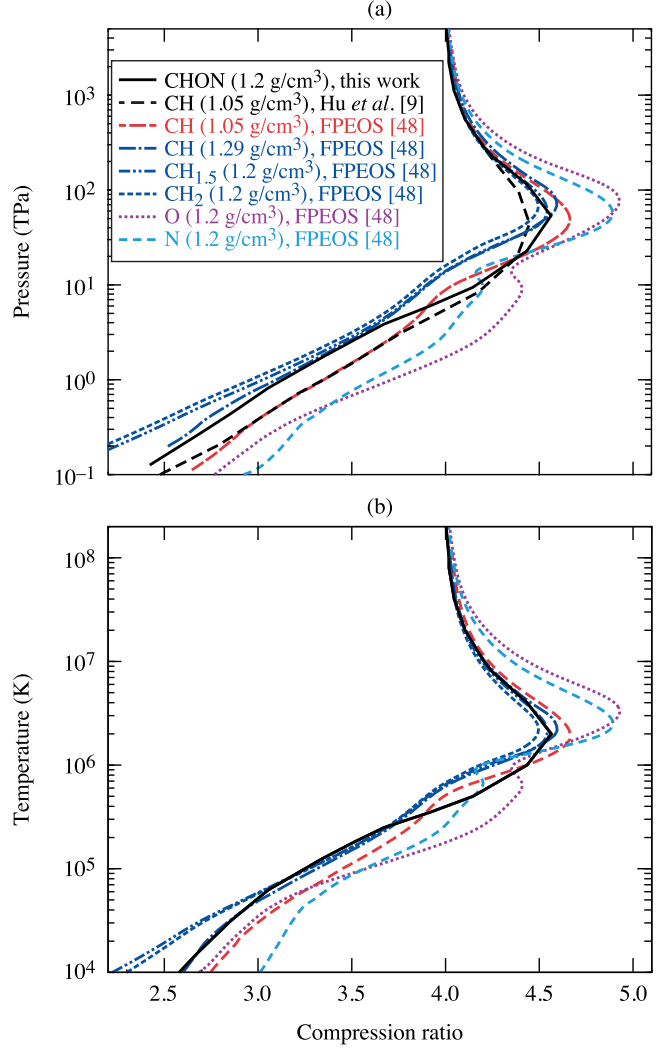
E304191J

FIG. 7. Comparison in pair-correlation functions from OF-DFT-MD and KS-DFT-MD calculations of CHON at selected densities and 250 000 K. The different sets of curves have been shifted apart for clarity. “bC”: bare-Coulomb.

flect changes in heat capacity; the differences between energy and pressure plots define the profile of the Grüneisen parameter. Both are due to the joint effects of ion thermal vibration and electron thermal excitation, which will be discussed later (Sec. III B).

Figure 6 shows our calculated and extrapolated EOS data as functions of density, in comparison with fully ionized ideal-gas (gray curves) and nonrelativistic Fermi degenerate electron gas (black lines) values at zero K [47], calculated via  $P_{\text{deg}} = 2n_e E_F / 5 = (3\pi^2)^{2/3} \hbar^2 / (5m_e) n_e^{5/3}$  and  $E_{\text{deg}} = 3P_{\text{deg}} V / 2$ , where  $\hbar$  is the reduced Planck constant,  $m_e$  is the electron mass,  $n_e$  is the electron number density, and  $V$  is the volume. The CHON system resembles the fully ionized ideal gas at above  $10^7$  K, for all densities considered in this study (0 to  $1044 \text{ g/cm}^3$ ). At lower temperatures and densities below  $0.1 \text{ g/cm}^3$ , the same scaling but quantitative disagreement with the fully ionized ideal-gas values indicate the system resembles an ideal gas that is partially ionized. The Fermi degeneracy limit is approached but not reached at the highest density of  $1044 \text{ g/cm}^3$ .

We have also compared the C–C, C–H, and H–H pair-correlation functions  $g(r)$  from our OF and KS simulations of CHON. Figure 7 shows OF-DFT MD reproduces the structureless or structured features in  $g(r)$  by KS-DFT MD at the matching conditions ( $250 \text{ 000 K}$ ). At  $25 \text{ g/cm}^3$ , the radial distribution results from KS-DFT-MD simulations with different electron–ion interaction potentials are consistent with each other. We note that the good agreement in  $g(r)$  at the matching conditions is not sufficient to justify the correspondence of KS and OF in the warm-dense-matter regime. In particular, the OF does not reproduce ionization effects of the shell electrons. This effect is not directly captured by the  $g(r)$  function but can lead to differences in the Hugoniot and thermodynamic properties, which are discussed in the following Sec. III B.

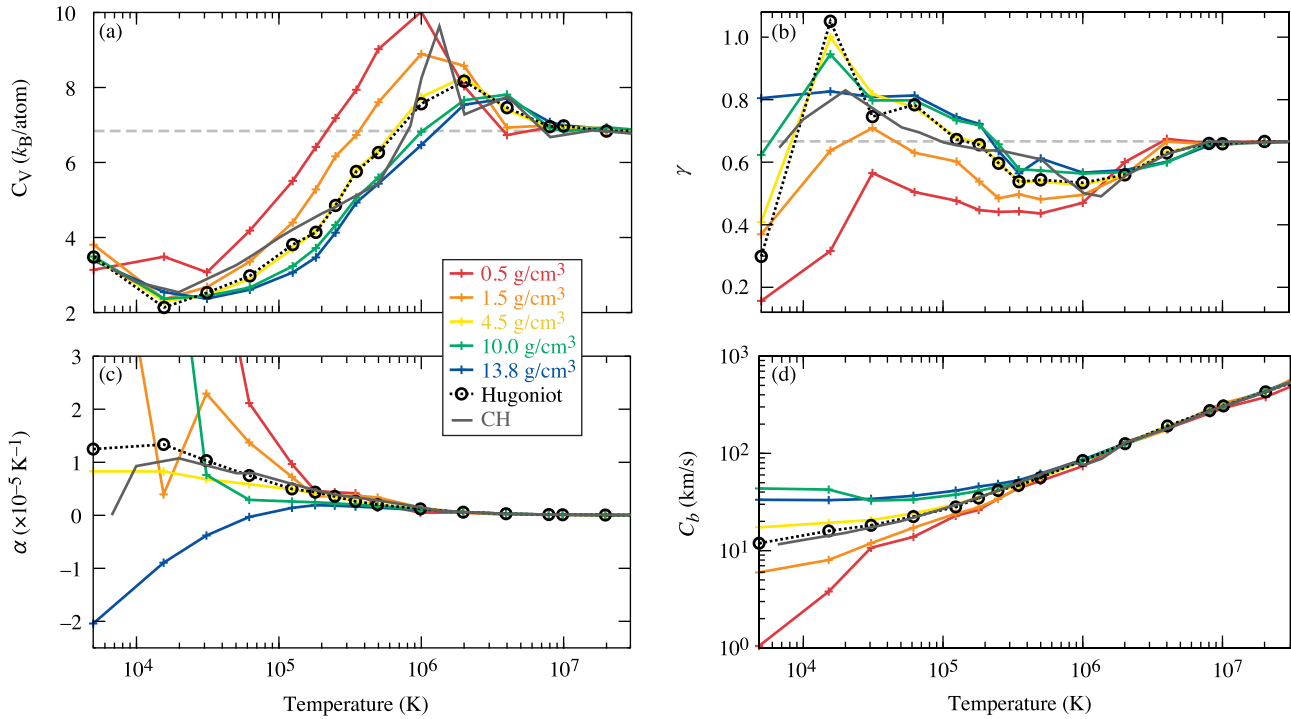


E304201J

FIG. 8. (a) Pressure- and (b) temperature-compression ratio Hugoniot of CHON compared with that of CH from KS/OF calculations and those of C–H compounds, O, and N from FPEOS.

### B. CHON versus CH: Hugoniot, thermodynamic properties, and bulk sound velocity

The shock Hugoniot of CHON can be straightforwardly calculated from the EOS table through the Rankine-Hugoniot equation,  $E - E_i + (P + P_i)(V - V_i)/2 = 0$ , where  $(E, P, V)$  denote the internal energy, pressure, and volume in the shocked state and  $(E_i, P_i, V_i)$  are the corresponding values at the initial unshocked state. By choosing CHON resin at ambient condition ( $1.2 \text{ g/cm}^3$  and  $298 \text{ K}$ ) as the initial state, the pressure and temperature Hugoniots as functions of compression ratio are calculated and compared to those of CH from KS/OF-DFT-MD [9] or KS-DFT-MD/path integral Monte Carlo (PIMC) [12,13,48] calculations and hydrocarbons, oxygen, and nitrogen from the first-principles EOS (FPEOS) database [48–50]. Figure 8 shows the CHON Hugoniot (black solid curve) up to  $3 \times 10^5 \text{ K}$  is close to that of KS-DFT-MD predictions of CH with a comparable initial density ( $1.29 \text{ g/cm}^3$ , blue dash-dotted curve), and the overall profile is



E30421J1

FIG. 9. (a) Heat capacity, (b) Grüneisen parameter, (c) thermal expansivity, and (d) bulk sound velocity of CHON as functions of temperature along selected isochores and the principal Hugoniot. Corresponding properties of pure CH along the polystyrene Hugoniot and calculated based on the FPEOS database [12,13,48] are shown in dark-gray solid curves for comparison. In (a) and (b), the horizontal gray dashed lines denote the corresponding values of a fully ionized ideal gas.

similar to that of the OF-DFT-MD predictions of CH (black dashed curve).

Figure 8 also shows that the OF-DFT-MD prediction of the CHON Hugoniot around the peak compression is narrower and has larger compression maximum (by  $\sim 2\%$ ) than pure CH. Based on estimations using the FPEOS database, the compression maxima of hydrocarbons are expected to increase with the C:H ratio (blue curves) or decrease with the initial density (blue dash-dotted versus red dotted curves), while pure nitrogen and oxygen have very high peak compression (pink and cyan curves). If the same trends are preserved for OF-DFT MD, we can attribute the observations about Hugoniot peak relations between CH (C:H = 1:1,  $\rho_i = 1.05$  g/cm $^3$ ) and CHON (C:H = 1:1.72,  $\rho_i = 1.2$  g/cm $^3$ ) to the inclusion of N and O in CHON. The all-electron PIMC Hugoniot for CH has been widely acknowledged to be accurate and shown to be consistent with experiments [11–14,51,52]. If a similar relation between PIMC and OF-DFT-MD predictions of the compression maxima of CH is expected for CHON, deduced by a 1.4% increase due to the use of LKT $\gamma$ TF (for CHON) rather than TF (for CH) functional (according to our tests), we estimate the real compression maximum of CHON to be  $\sim 4.7$  and occur at 50 TPa and  $2 \times 10^6$  K. This can be verified by alternative methods, such as PIMC [48], spectral quadrature [53–56], extended DFT [51,57–59] or hybrid Kohn-Sham+Thomas-Fermi [60], that improve the description of core electrons at such high temperatures, and tested in future experiments on gigabar (Gbar) platforms such as the National Ignition Facility [14].

To better understand the differences between CHON and CH, and for applications to planetary modeling and comparisons with future experiments, we have calculated the thermodynamic parameters and sound velocities of CHON based on our EOS. These include the heat capacity

$$C_V = (\partial E / \partial T)_V,$$

the Grüneisen parameter

$$\gamma = V(\partial P / \partial E)_V,$$

the thermal expansion coefficient

$$\alpha = (\partial \ln V / \partial T)_P = -(\partial \ln \rho / \partial T)_P,$$

and the bulk sound velocity

$$C_b = \sqrt{K_S / \rho} = \sqrt{K_T(1 + \alpha\gamma T) / \rho},$$

where

$$K_T = -V(\partial P / \partial V)_T = (\partial P / \partial \ln \rho)_T$$

is the isothermal bulk modulus that must be corrected to the adiabatic bulk modulus  $K_S$  to compare with experiments. This approach has been applied to study shocked-compressed silica and shown to predict similar properties as those measured by experiments [61].

Figure 9 summarizes the calculated thermodynamic properties and sound velocity of CHON along five different isochores (colored curves) and along the Hugoniot (dashed line-circles), in comparison with those for CH polystyrene along its Hugoniot (gray curves). Setting aside the fluctuations

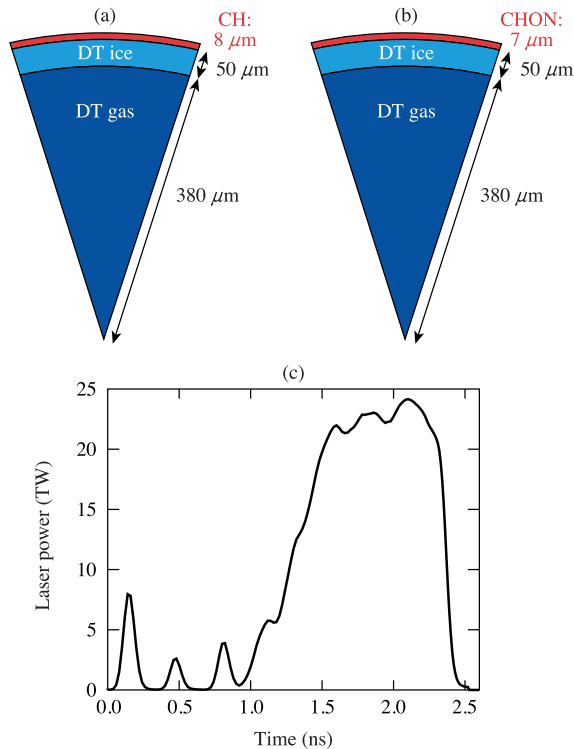


FIG. 10. Target assemblies using (a) CH or (b) CHON as the ablator, and (c) laser pulse shape used in our *LILAC* simulations.

at low temperatures, which are due to the sensitivity of the derivatives to the nonsmoothness of the numerical EOS data, the results clearly show the following trends: (1)  $C_V$  exceeds the “Dulong-Petit” limit of  $3k_B/\text{atom}$  (classical high-temperature limit for solids) at 5000 K, decreases with temperature, and shows a minimum at  $2$  to  $3 \times 10^4$  K, then increases to show a peak at  $10^6$  K, and finally approaches the fully ionized ideal gas limit value of  $6.84 k_B/\text{atom}$  ( $=1.5 k_B/\text{particle} \times 228 \text{ particles}/50 \text{ atoms}$ ) at above  $10^7$  K; (2)  $\gamma$  seems to show opposite trends as  $C_V$ —it first increases and reaches a maximum at  $2$  to  $3 \times 10^4$  K, then decreases and shows a minimum at  $10^6$  K, and eventually approaches the limit of  $2/3$ ; (3)  $\alpha$  and  $C_b$  are sensitive to density at temperatures below  $10^5$  K and almost independent of density at  $10^6$  K or higher; and (4) the results of CHON resin along the Hugoniot are overall similar to that of CH polystyrene.

We note that the minimum in  $C_V$  has been observed in other materials under high temperature, pressure conditions and attributed to a transition of the system from a bonded to an atomic fluid [62,63]. Structural changes by chemical bond dissociation in the CHON liquid are associated with the decreasing  $C_V$  and increasing  $\gamma$  below  $2$  to  $3 \times 10^4$  K (or approximately 4 Mbar and  $3.4 \text{ g/cm}^3$  along the Hugoniot). Beyond these conditions electron thermal excitation dominates, leading to the peak in  $C_V$  and valley in  $\gamma$  before they turn around (as  $K$  shell ionization is completing) at  $10^6$  K ( $\sim 228$  Mbar and  $5.3 \text{ g/cm}^3$  along the Hugoniot) and reach the fully ionized ideal gas limit at  $10^7$  K ( $\sim 2.85$  Gbar, or 285 TPa, along the Hugoniot).

We also note that the Grüneisen parameter is important in constructing empirical EOS and planetary impact

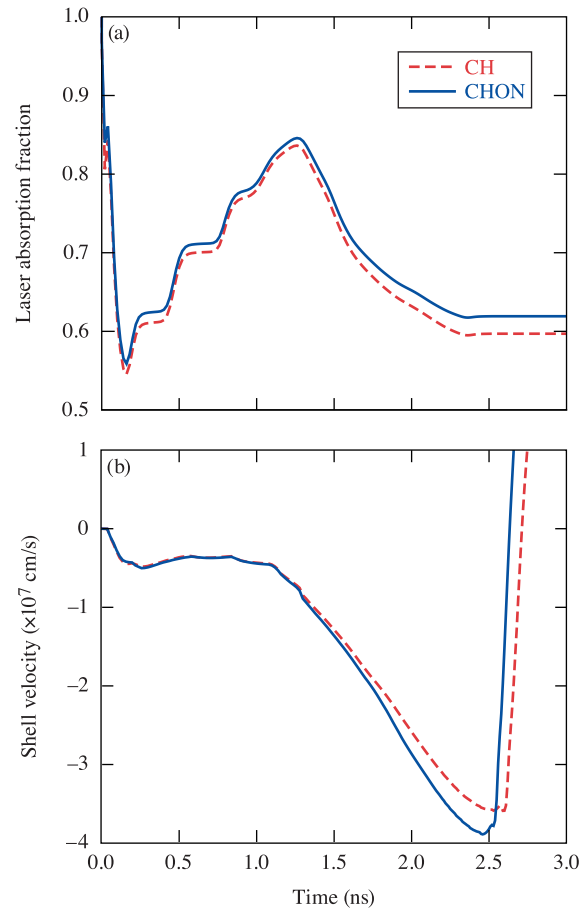


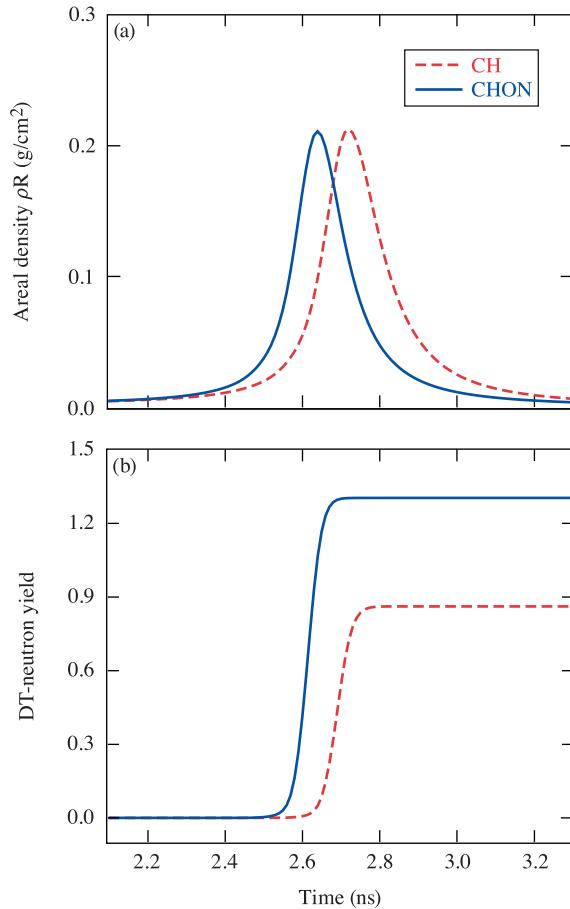
FIG. 11. Comparison in the time evolution of (a) laser absorption fraction and (b) implosion velocity between targets using CH or CHON as the ablator.

models [64,65]. Our findings about the existence of a basin structure in the Grüneisen parameter of CHON before it reaches the limit of  $2/3$  is consistent with previous calculations for  $\text{MgSiO}_3$  [66]. The decrease in the Grüneisen parameter along the Hugoniot at  $10^4$  to  $10^5$  K has also been observed in shock experiments on  $\text{SiO}_2$  and  $\text{MgSiO}_3$  fluids [61,67,68]. At lower temperatures (below  $\sim 2 \times 10^4$  K, 3 Mbar, or  $3.3 \text{ g/cm}^3$ ), the Grüneisen parameter increases, similar to previous experimental and theoretical reports for CH and  $\text{MgSiO}_3$  at relatively low pressures [67,69]. More experiments with improved accuracy are still desired to benchmark the theoretical predictions.

### C. Radiation-hydrodynamic simulations of ICF implosions with a CHON ablator

To test the laser absorption and hydrodynamic efficiency of CHON resin as a potential ablator material for LDD targets, we have performed radiation-hydrodynamic simulations of cryogenic DT implosion targets by using the 1-D radiation-hydrodynamics code *LILAC* [70]. The CHON results are compared with the conventional polystyrene (CH:  $\text{C}_{42}\text{H}_{58}$ ) ablator. State-of-the-art physics models are employed in these simulations, including ray-tracing for laser energy deposition



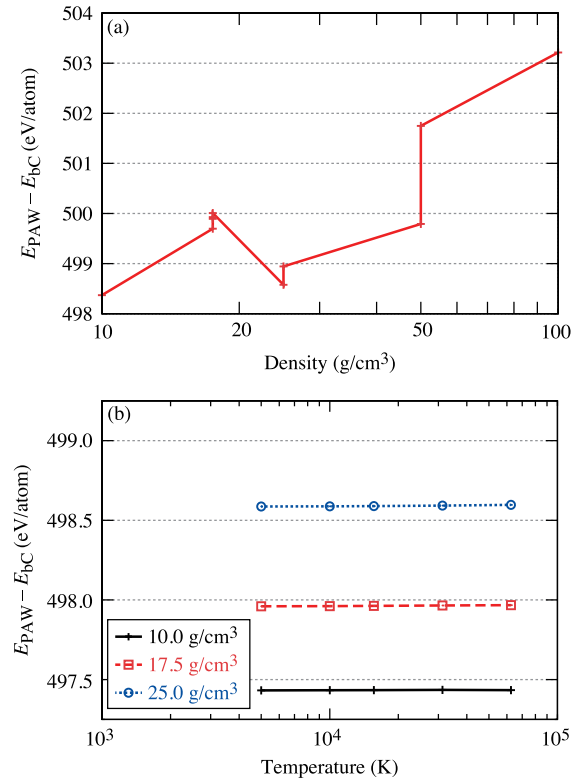


E30424J1

FIG. 12. Comparison in (a) areal density and (b) neutron yield at later time of the implosion when using targets with CH or CHON ablaters.

with a cross-beam energy transfer model [71], nonlocal thermal transport model of iSNB [72], and the first-principles equation-of-state [9,73,74] and opacity tables [75,76] for constituent materials of DT and CH. For CHON we use the first-principles EOS table created in this work, while a collisional-radiative-equilibrium model [77] is applied for the opacity of CHON. A typical OMEGA-scale cryo-DT target displayed in Fig. 10(a) consists of a  $50\text{-}\mu\text{m}$ -thick DT-ice layer covered by  $8\text{-}\mu\text{m}$ -thick CH ablator ( $\rho_0 = 1.05 \text{ g/cm}^3$ ). To have a mass-equivalent target with a CHON ablator ( $\rho_0 = 1.2 \text{ g/cm}^3$ ), Figure 10(b) shows the CHON-layer thickness is slightly reduced to  $7 \mu\text{m}$  (due to its higher density). We conducted LILAC simulations for these two targets imploded by the same laser pulse depicted by Fig. 10(c), having a total UV laser energy of  $\sim 27 \text{ kJ}$  on OMEGA.

The LILAC simulation results are presented in Figs. 11 and 12 with comparisons between CH-ablator (red/dashed curve) and CHON-ablator (blue/solid curve) cases. Figure 11(a) shows the accumulative laser absorption fraction during the implosion, in which the CHON-ablator case gives slightly ( $\sim 2\%$ ) more laser absorption than the CH-ablator case. This can be explained by the larger effective charge of  $Z_{\text{eff}} = \langle Z^2 \rangle / \langle Z \rangle \approx 5.82$  for CHON than the value of  $Z_{\text{eff}} \approx 5.06$  of CH, because the inverse Bremsstrahlung laser



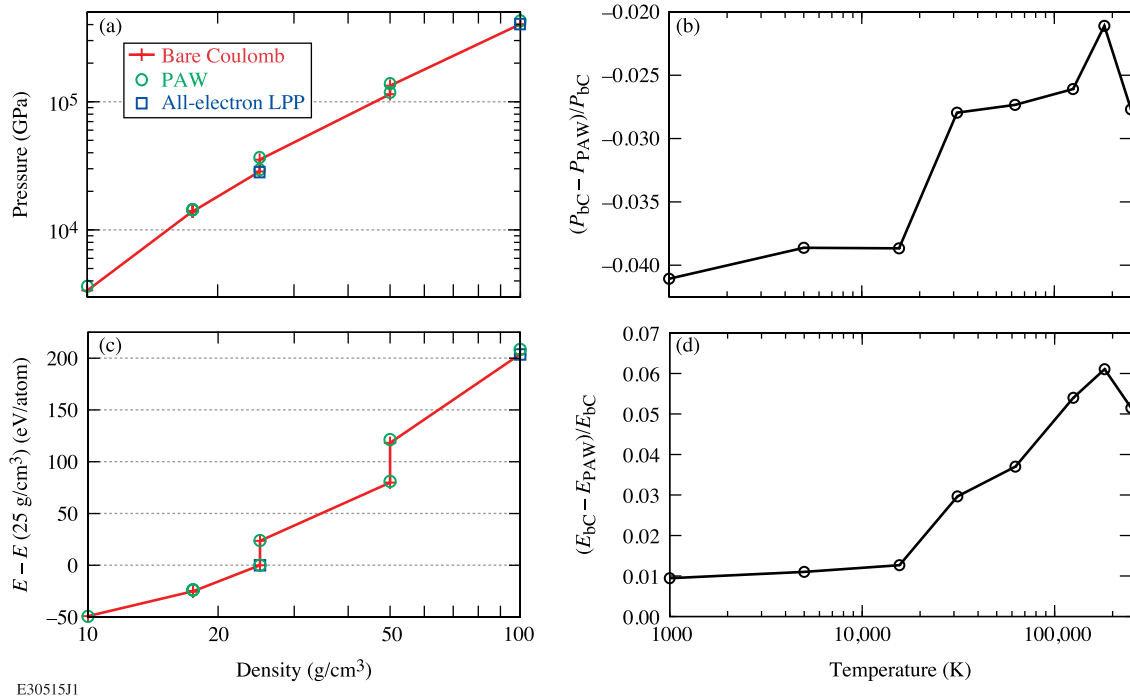
E30514J1

FIG. 13. Energy differences between PAW and bare-Coulomb calculations for single snapshots as a function of (a) density and (b) electronic temperature. In (a), the electronic temperature is  $1000 \text{ K}$  in all cases except  $17.5 \text{ g/cm}^3$ , which includes results from extra calculations at  $15,625 \text{ K}$  or using a  $2 \times 2 \times 2 k$  mesh, as compared to only using the  $\Gamma$  point in other cases. Differences between (a) and (b) at comparable density-temperature conditions are negligible and are due to differences in snapshots and detailed settings of the calculations. “bC”: bare-Coulomb.

absorption depends on  $Z_{\text{eff}}$ . The time-dependent implosion velocity ( $v_{\text{imp}}$ ) comparison is illustrated in Fig. 11(b), which shows  $\sim 9\%$  increase in  $v_{\text{imp}}$  for the CHON case. This enhanced implosion velocity can be attributed to the  $\sim 2\%$  increase of laser absorption [Fig. 11(a)] as well as the slightly larger value of  $\langle A \rangle / \langle Z \rangle = 1.85$  for CHON, improving the hydrodynamic efficiency.

Figure 12 compares the LILAC-predicted target performance for the two implosions using CH and CHON ablaters. Figure 12(a) shows the compression areal density ( $\rho R$ ) as a function of time. Both targets give very similar peak compression of  $\sim 210 \text{ mg/cm}^2$ , though the bang time is  $\sim 100 \text{ ps}$  earlier for the CHON case due to its higher implosion velocity. The  $\sim 9\%$  increase of  $v_{\text{imp}}$  for the CHON-ablator case leads to  $\sim 46\%$  higher neutron yield seen in Fig. 12(b). The neutron yield changes from  $8.8 \times 10^{13}$  for CH to  $1.3 \times 10^{14}$  for CHON. Overall, we find CHON resin is a moderately better ablator material for LDD target designs. This will prompt us to further pursue the use of CHON resin for 3-D-printed LDD capsules with a foam layer for laser-imprint mitigation [3].

It is noted that the CH target was designed for OMEGA shots to reach hot-spot pressure of  $80 \text{ Gbar}$ ; it was therefore tuned for good shock timing. Using the same laser pulse



E30515J1

FIG. 14. Comparison in (a),(b) pressure and (c),(d) energy calculated by KS calculations using different potentials. Results in (a) and (c) are based on single-snapshot KS-DFT calculations for the same structures and electronic temperatures as Fig. 13(a). Results in (b) and (d) are based on KS-DFT-MD calculations at  $25 \text{ g/cm}^3$ . “bC”: bare-Coulomb.

shape, the CHON target “suffers” only very small mistiming, after all the ablator thickness differs only by  $1 \mu\text{m}$ . Even with such a small mistiming of shocks, the CHON target performs better than the shock-timing-optimized CH target. Of course, one can fine-tune shocks for the CHON target so that an even better performance can be resulted. However, that is not the main purpose of this paper. Finally, our simulation tests show that the slight difference in opacity models available for CH and CHON is not the source for the observed performance difference. Again, the performance difference comes from the higher laser absorption and better hydro-efficiency of CHON.

#### IV. CONCLUSIONS

In this work, we have constructed a wide-range, self-coherent (with errors between different computational approaches up to  $\sim 6\%$ ) EOS table for  $\text{CH}_{1.72}\text{O}_{0.37}\text{N}_{0.086}$  based on first-principles calculations (KS+OF-DFT MD) and numerical extrapolation [78]. Our predicted Hugoniot of CHON resin shows a sharper profile and larger compression maximum by  $\sim 2\%$  than that of pure CH polystyrene, due to the coexistence of nitrogen and oxygen. Calculations of thermodynamic properties show overall consistency with that of CH along their respective Hugoniots. Both exhibit a local minimum in heat capacity and maximum in the Grüneisen parameter at  $2$  to  $3 \times 10^4 \text{ K}$ , which corresponds to chemical bond dissociation, and a peak in heat capacity and a basin in the Grüneisen parameter at  $10^6 \text{ K}$ , corresponding to ionization of the  $K$  shell. The heat capacity and the Grüneisen parameters are found to reach the fully ionized ideal gas limit at  $10^7 \text{ K}$ , while the thermal expansion coefficient and the bulk sound

velocity show independence of the isochore once temperature exceeds  $10^6 \text{ K}$ . 1D radiation hydrodynamic simulations show CHON resin outperforms CH polystyrene as an ablator material for laser-direct-drive target designs, due to slight increase in the laser absorption fraction. This further prompts the TPP fabrication of the CHON shell with a foam layer for laser-imprint mitigation.

#### ACKNOWLEDGMENTS

This material is based upon work supported by the Department of Energy National Nuclear Security Administration under Award No. DE-NA0003856, the University of Rochester, and the New York State Energy Research and Development Authority. V.V.K., D.I.M., R.M.N.G., and S.X.H. also acknowledge support by the US NSF PHY Grants No. 1802964 and No. 2205521.

This report was prepared as an account of work sponsored by an agency of the U.S. Government. Neither the U.S. Government nor any agency thereof, nor any of their employees, makes any warranty, express or implied, or assumes any legal liability or responsibility for the accuracy, completeness, or usefulness of any information, apparatus, product, or process disclosed, or represents that its use would not infringe privately owned rights. Reference herein to any specific commercial product, process, or service by trade name, trademark, manufacturer, or otherwise does not necessarily constitute or imply its endorsement, recommendation, or favoring by the U.S. Government or any agency thereof. The views and opinions of authors expressed herein do not necessarily state or reflect those of the U.S. Government or any agency thereof.

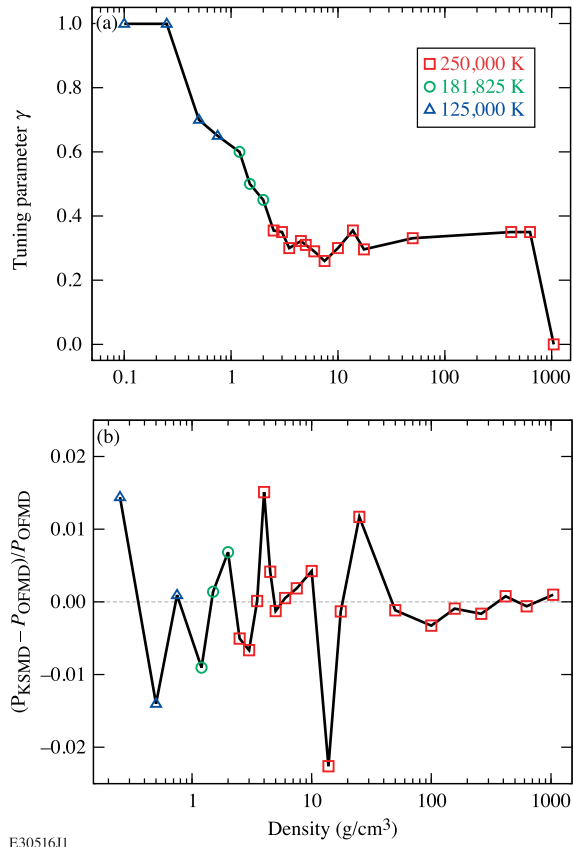


FIG. 15. (a) Tuning parameters  $\gamma$  determined in this study for CHON at different densities. The matching temperature is shown in the legend. (b) Relative differences in pressure between OF- and KS-DFT MD at the matching condition.

## APPENDIX: MORE TECHNICAL DETAILS

### 1. Aligning bare-Coulomb with PAW energies

Figure 13 shows the energy difference between the bare-Coulomb and PAW calculations is approximately 500 eV/atom at various densities, nearly independent of temperature.

### 2. Validation of bare-Coulomb potentials

Figure 14 shows PAW and bare-Coulomb calculations produce EOS for CHON that agree within 1%–6%. In addition, we found good agreements between bare-Coulomb and all-electron LPP results. These validate our choice of bare-Coulomb potentials at 25 g/cm<sup>3</sup> or higher densities.

### 3. Tuning parameter in LKT $\gamma$ TF calculations

Figure 15 shows values of  $\gamma$ , the matching conditions, and a comparison in pressure between KS- and OF-DFT MD at

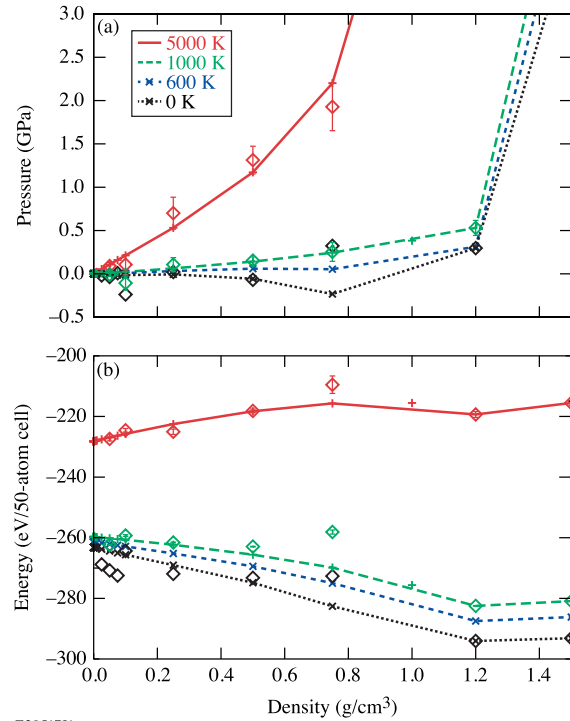


FIG. 16. (a) Pressures and (b) internal energies at relatively low densities along four different isotherms. KS-DFT(MD) data are shown with diamond symbols for comparison.

the matching condition determined for CHON in this study. Our additional tests show the fluctuation in the  $\gamma$ -density plot [Fig. 15(a)] leads to errors in pressure of up to 2% (at the matching condition) or smaller (at above the matching temperatures).

### 4. EOS at low densities

Figure 16 shows the low-density region of the CHON EOS table constructed in this work (line-crosses), in comparison to data from KS-DFT (at 0 K) and KS-DFT-MD (at 1000 and 5000 K) calculations (diamond symbols). The overall agreement between the tabulated and the calculated data at 1000 and 5000 K indicates the Redlich-Kwong fit works well. Scattering of the calculated data at 0 K reflects the sensitivity of the low-density EOS to the structure models, which is a challenge to first-principles calculations because of the limitations by the cell size and the computational cost. In this work, we use numerical extrapolation or interpolation to estimate the EOS at 0, 150, 298, and 600 K for the purpose of making the EOS table practically useful for radiation-hydrodynamic simulations. The errors in the low-density, low-temperature region of the table is not a concern for typical ICF applications (see conditions charted in, e.g., Fig. 1 in Ref. [79]).

[1] R. S. Craxton, K. S. Anderson, T. R. Boehly, V. N. Goncharov, D. R. Harding, J. P. Knauer, R. L. McCrory, P. W. McKenty,

D. D. Meyerhofer, J. F. Myatt, A. J. Schmitt, J. D. Sethian, R. W. Short, S. Skupsky, W. Theobald, W. L. Kruer, K. Tanaka,

- R. Betti, T. J. B. Collins, J. A. Delettrez *et al.*, Direct-drive inertial confinement fusion: A review, *Phys. Plasmas* **22**, 110501 (2015).
- [2] J. Lindl, Development of the indirect drive approach to inertial confinement fusion and the target physics basis for ignition and gain, *Phys. Plasmas* **2**, 3933 (1995).
- [3] S. X. Hu, W. Theobald, P. B. Radha, J. L. Peebles, S. P. Regan, A. Nikroo, M. J. Bonino, D. R. Harding, V. N. Goncharov, N. Petta, T. C. Sangster, and E. M. Campbell, Mitigating laser-imprint effects in direct-drive inertial confinement fusion implosions with an above-critical-density foam layer, *Phys. Plasmas* **25**, 082710 (2018).
- [4] N. Metzler, A. L. Velikovich, and J. H. Gardner, Reduction of early-time perturbation growth in ablatively driven laser targets using tailored density profiles, *Phys. Plasmas* **6**, 3283 (1999).
- [5] M. Barrios, D. Hicks, T. Boehly, D. Fratanduono, J. Eggert, P. Celliers, G. Collins, and D. Meyerhofer, High-precision measurements of the equation of state of hydrocarbons at 1–10 mbar using laser-driven shock waves, *Phys. Plasmas* **17**, 056307 (2010).
- [6] S. Hamel, L. X. Benedict, P. M. Celliers, M. A. Barrios, T. R. Boehly, G. W. Collins, T. Döppner, J. H. Eggert, D. R. Farley, D. G. Hicks, J. L. Kline, A. Lazicki, S. LePape, A. J. Mackinnon, J. D. Moody, H. F. Robey, E. Schwegler, and P. A. Sterne, Equation of state of ch 1.36: First-principles molecular dynamics simulations and shock-and-release wave speed measurements, *Phys. Rev. B* **86**, 094113 (2012).
- [7] C. Wang, X.-T. He, and P. Zhang, Thermophysical properties for shock compressed polystyrene, *Phys. Plasmas* **18**, 082707 (2011).
- [8] S. X. Hu, T. R. Boehly, and L. A. Collins, Properties of warm dense polystyrene plasmas along the principal hugoniot, *Phys. Rev. E* **89**, 063104 (2014).
- [9] S. X. Hu, L. A. Collins, V. N. Goncharov, J. D. Kress, R. L. McCrory, and S. Skupsky, First-principles equation of state of polystyrene and its effect on inertial confinement fusion implosions, *Phys. Rev. E* **92**, 043104 (2015).
- [10] P. Colin-Lalu, V. Recoules, G. Salin, T. Plisson, E. Brambrink, T. Vinci, R. Bolis, and G. Huser, Dissociation along the principal hugoniot of the laser mégajoule ablator material, *Phys. Rev. E* **94**, 023204 (2016).
- [11] T. Döppner, D. C. Swift, A. L. Kritcher, B. Bachmann, G. W. Collins, D. A. Chapman, J. Hawreliak, D. Kraus, J. Nilsen, S. Rothman *et al.*, Absolute Equation-of-State Measurement for Polystyrene from 25 to 60 Mbar Using a Spherically Converging Shock Wave, *Phys. Rev. Lett.* **121**, 025001 (2018).
- [12] S. Zhang, K. P. Driver, F. Soubiran, and B. Militzer, First-principles equation of state and shock compression predictions of warm dense hydrocarbons, *Phys. Rev. E* **96**, 013204 (2017).
- [13] S. Zhang, B. Militzer, L. X. Benedict, F. Soubiran, P. A. Sterne, and K. P. Driver, Path integral Monte Carlo simulations of dense carbon-hydrogen plasmas, *J. Chem. Phys.* **148**, 102318 (2018).
- [14] A. L. Kritcher, D. C. Swift, T. Döppner, B. Bachmann, L. X. Benedict, G. W. Collins, J. L. DuBois, F. Elsner, G. Fontaine, J. A. Gaffney, S. Hamel, A. Lazicki, W. R. Johnson, N. Kostinski, D. Kraus, M. J. MacDonald, B. Maddox, M. E. Martin, P. Neumayer, A. Nikroo *et al.*, A measurement of the equation of state of carbon envelopes of white dwarfs, *Nature (London)* **584**, 51 (2020).
- [15] O. Stein, Y. Liu, J. Streit, J. H. Campbell, Y. F. Lu, Y. Aglitskiy, and N. Petta, Fabrication of low-density shock-propagation targets using two-photon polymerization, *Fusion Sci. Technol.* **73**, 153 (2018).
- [16] Polymer 3D models: Monomer 3D models, Polymers Up Close and Personal, Accessed 8 August 2021, <https://pslc.ws/modelhtml/poly3D.htm>.
- [17] Our structure model ( $C_{16}H_{27}O_6N_1$ ) has per-mole percentages of 32%, 54%, 12%, and 2% of C, H, O, and N, respectively. These are very close to values (31.5%, 54.2%, 11.6%, 2.7%) in the empirical formula  $CH_{1.72}O_{0.37}N_{0.086}$ . The stoichiometry differences are below 0.7% for all elements, and the difference in  $\langle Z \rangle$  is less than 0.3% (3.56 vs 3.55). In comparison to the errors in the EOS data (up to  $\sim 6\%$ ), this stoichiometry and  $\langle Z \rangle$  differences are negligible.
- [18] P. Hohenberg and W. Kohn, Inhomogeneous electron gas, *Phys. Rev.* **136**, B864 (1964).
- [19] W. Kohn and L. J. Sham, Self-consistent equations including exchange and correlation effects, *Phys. Rev.* **140**, A1133 (1965).
- [20] J. Sun, A. Ruzsinszky, and J. P. Perdew, Strongly Constrained and Appropriately Normed Semilocal Density Functional, *Phys. Rev. Lett.* **115**, 036402 (2015).
- [21] G. Kresse and J. Furthmüller, Efficient iterative schemes for ab initio total-energy calculations using a plane-wave basis set, *Phys. Rev. B* **54**, 11169 (1996).
- [22] V. V. Karasiev, D. I. Mihaylov, and S. X. Hu, Meta-GGA exchange-correlation free energy density functional to increase the accuracy of warm dense matter simulations, *Phys. Rev. B* **105**, L081109 (2022).
- [23] D. Mejia-Rodriguez and S. B. Trickey, Deorbitalization strategies for meta-generalized-gradient-approximation exchange-correlation functionals, *Phys. Rev. A* **96**, 052512 (2017).
- [24] P. E. Blöchl, O. Jepsen, and O. K. Andersen, Improved tetrahedron method for Brillouin-zone integrations, *Phys. Rev. B* **49**, 16223 (1994).
- [25] The “bare-Coulomb” potentials for C, O, and N were generated by modifying that for H, which was supplied by VASP. The modifications include the number of electrons, atomic mass, energy of the pseudoatom, and the default cutoff energy.
- [26] P. Giannozzi, S. Baroni, N. Bonini, M. Calandra, R. Car, C. Cavazzoni, D. Ceresoli, G. L. Chiarotti, M. Cococcioni, I. Dabo, A. D. Corso, S. de Gironcoli, S. Fabris, G. Fratesi, R. Gebauer, U. Gerstmann, C. Gougoussis, A. Kokalj, M. Lazzeri, L. Martin-Samos *et al.*, QUANTUM ESPRESSO: A modular and open-source software project for quantum simulations of materials, *J. Phys.: Condens. Matter* **21**, 395502 (2009).
- [27] S. X. Hu, Continuum Lowering and Fermi-Surface Rising in Strongly Coupled and Degenerate Plasmas, *Phys. Rev. Lett.* **119**, 065001 (2017).
- [28] D. I. Mihaylov, V. V. Karasiev, S. X. Hu, J. R. Rygg, V. N. Goncharov, and G. W. Collins, Improved first-principles equation-of-state table of deuterium for high-energy-density applications, *Phys. Rev. B* **104**, 144104 (2021).
- [29] K. Lejaeghere, G. Bihlmayer, T. Bjorkman, P. Blaha, S. Blugel, V. Blum, D. Caliste, I. E. Castelli, S. J. Clark, A. Dal Corso, S. de Gironcoli, T. Deutsch, J. K. Dewhurst, I. Di Marco, C. Draxl, M. Du ak, O. Eriksson, J. A. Flores-Livas, K. F.

- Garrity, L. Genovese *et al.*, Reproducibility in density functional theory calculations of solids, *Science* **351**, aad3000 (2016).
- [30] A. Baldereschi, Mean-value point in the Brillouin zone, *Phys. Rev. B* **7**, 5212 (1973).
- [31] S. Nosé, A unified formulation of the constant temperature molecular dynamics methods, *J. Chem. Phys.* **81**, 511 (1984).
- [32] W. G. Hoover, Canonical dynamics: Equilibrium phase-space distributions, *Phys. Rev. A* **31**, 1695 (1985).
- [33] N. D. Mermin, Thermal properties of the inhomogeneous electron gas, *Phys. Rev.* **137**, A1441 (1965).
- [34] V. V. Karasiev, J. Hinz, and D. I. Mihaylov, Tunable noninteracting free-energy functionals (unpublished).
- [35] K. Luo, V. V. Karasiev, and S. B. Trickey, Towards accurate orbital-free simulations: A generalized gradient approximation for the noninteracting free energy density functional, *Phys. Rev. B* **101**, 075116 (2020).
- [36] R. P. Feynman, N. Metropolis, and E. Teller, Equations of state of elements based on the generalized fermi-thomas theory, *Phys. Rev.* **75**, 1561 (1949).
- [37] S. X. Hu, B. Militzer, L. A. Collins, K. P. Driver, and J. D. Kress, First-principles prediction of the softening of the silicon shock hugoniot curve, *Phys. Rev. B* **94**, 094109 (2016).
- [38] S. X. Hu, R. Gao, Y. Ding, L. A. Collins, and J. D. Kress, First-principles equation-of-state table of silicon and its effects on high-energy-density plasma simulations, *Phys. Rev. E* **95**, 043210 (2017).
- [39] Y. H. Ding and S. X. Hu, First-principles equation-of-state table of beryllium based on density-functional theory calculations, *Phys. Plasmas* **24**, 062702 (2017).
- [40] C. Hartwigsen, S. Goedecker, and J. Hutter, Relativistic separable dual-space Gaussian pseudopotentials from H to Rn, *Phys. Rev. B* **58**, 3641 (1998).
- [41] V. V. Karasiev, T. Sjostrom, and S. B. Trickey, Generalized-gradient-approximation noninteracting free-energy functionals for orbital-free density functional calculations, *Phys. Rev. B* **86**, 115101 (2012).
- [42] F. Lambert, J. Clérouin, and G. Zérah, Very-high-temperature molecular dynamics, *Phys. Rev. E* **73**, 016403 (2006).
- [43] A. Willand, Y. O. Kvashnin, L. Genovese, A. Vázquez-Mayagoitia, A. K. Deb, A. Sadeghi, T. Deutsch, and S. Goedecker, Norm-conserving pseudopotentials with chemical accuracy compared to all-electron calculations, *J. Chem. Phys.* **138**, 104109 (2013).
- [44] V. V. Karasiev, T. Sjostrom, and S. B. Trickey, Finite-temperature orbital-free DFT molecular dynamics: Coupling PROFESS and QUANTUM ESPRESSO, *Comput. Phys. Commun.* **185**, 3240 (2014).
- [45] O. Redlich and J. N. S. Kwong, On the thermodynamics of solutions. V. An equation of state. Fugacities of gaseous solutions, *Chem. Rev.* **44**, 233 (1949).
- [46] Note that the cold curve is calculated by using the SCAN functional, which outperforms T-SCAN-L in reaching convergence in the self-consistent functional calculations. The resultant energies have been uniformly shifted by the difference (23.6 eV/50-atom cell) from a T-SCAN-L calculation at 1.2 g/cm<sup>3</sup> and 0 K.
- [47] S. Eliezer, A. Ghatak, and H. Hora, *Fundamentals of Equations of State* (World Scientific, Singapore, 2002).
- [48] B. Militzer, F. González-Cataldo, S. Zhang, K. P. Driver, and F. Soubiran, First-principles equation of state database for warm dense matter computation, *Phys. Rev. E* **103**, 013203 (2021).
- [49] K. P. Driver and B. Militzer, First-principles equation of state calculations of warm dense nitrogen, *Phys. Rev. B* **93**, 064101 (2016).
- [50] K. P. Driver, F. Soubiran, S. Zhang, and B. Militzer, First-principles equation of state and electronic properties of warm dense oxygen, *J. Chem. Phys.* **143**, 164507 (2015).
- [51] X. Liu, X. Zhang, C. Gao, S. Zhang, C. Wang, D. Li, P. Zhang, W. Kang, W. Zhang, and X. T. He, Equations of state of poly- $\alpha$ -methylstyrene and polystyrene: First-principles calculations versus precision measurements, *Phys. Rev. B* **103**, 174111 (2021).
- [52] S. Zhang, M. C. Marshall, L. H. Yang, P. A. Sterne, B. Militzer, M. Däne, J. A. Gaffney, A. Shamp, T. Ogitsu, K. Caspersen, A. E. Lazicki, D. Erskine, R. A. London, P. M. Celliers, J. Nilsen, and H. D. Whitley, Wide-Ranging Equations of State for B4C Constrained by Theoretical Calculations and Shock Experiments, *LLE Review Quarterly Report* **164**, 198 Laboratory for Laser Energetics, University of Rochester, Rochester, NY, LLE Document No. DOE/NA/3856-1602 (2021).
- [53] P. Suryanarayana, On spectral quadrature for linear-scaling density functional theory, *Chem. Phys. Lett.* **584**, 182 (2013).
- [54] P. Suryanarayana, P. P. Pratapa, A. Sharma, and J. E. Pask, Sqdft: Spectral quadrature method for large-scale parallel O(N) KohnSham calculations at high temperature, *Comput. Phys. Commun.* **224**, 288 (2018).
- [55] S. Zhang, A. Lazicki, B. Militzer, L. H. Yang, K. Caspersen, J. A. Gaffney, M. W. Däne, J. E. Pask, W. R. Johnson, A. Sharma, P. Suryanarayana, D. D. Johnson, A. V. Smirnov, P. A. Sterne, D. Erskine, R. A. London, F. Coppari, D. Swift, J. Nilsen, A. J. Nelson *et al.*, Equation of state of boron nitride combining computation, modeling, and experiment, *Phys. Rev. B* **99**, 165103 (2019).
- [56] M. Bethkenhagen, A. Sharma, P. Suryanarayana, J. E. Pask, B. Sadigh, and S. Hamel, Thermodynamic, structural, and transport properties of dense carbon up to 10 million kelvin from kohn-sham density functional theory calculations, [arXiv:2110.01034](https://arxiv.org/abs/2110.01034) (2021).
- [57] S. Zhang, H. Wang, W. Kang, P. Zhang, and X. T. He, Extended application of kohn-sham first-principles molecular dynamics method with plane wave approximation at high energy—from cold materials to hot dense plasmas, *Phys. Plasmas* **23**, 042707 (2016).
- [58] A. Blanchet, J. Clérouin, M. Torrent, and F. Soubiran, Extended first-principles molecular dynamics model for high temperature simulations in the abinit code: Application to warm dense aluminum, *Comput. Phys. Commun.* **271**, 108215 (2022).
- [59] A. Blanchet, F. Soubiran, M. Torrent, and J. Clérouin, Extended first-principles molecular dynamics simulations of hot dense boron: equation of state and ionization, *Contrib. Plasma Phys.* **e202100234** (2022).
- [60] P. Hollebon and T. Sjostrom, Hybrid Kohn-Sham + Thomas-Fermi scheme for high-temperature density functional theory, *Phys. Rev. B* **105**, 235114 (2022).

- [61] M. Li, S. Zhang, H. Zhang, G. Zhang, F. Wang, J. Zhao, C. Sun, and R. Jeanloz, Continuous Sound Velocity Measurements along the Shock Hugoniot Curve of Quartz, *Phys. Rev. Lett.* **120**, 215703 (2018).
- [62] D. G. Hicks, T. R. Boehly, J. H. Eggert, J. E. Miller, P. M. Celliers, and G. W. Collins, Dissociation of Liquid Silica at High Pressures and Temperatures, *Phys. Rev. Lett.* **97**, 025502 (2006).
- [63] S. Zhang, M. A. Morales, R. Jeanloz, M. Millot, S. X. Hu, and E. Zurek, Nature of the bonded-to-atomic transition in liquid silica to tpa pressures, *J. Appl. Phys.* **131**, 071101 (2022).
- [64] S. Stewart, E. Davies, M. Duncan, S. Lock, S. Root, J. Townsend, R. Kraus, R. Caracas, and S. Jacobsen, The shock physics of giant impacts: Key requirements for the equations of state, *AIP Conf. Proc.* **2272**, 080003 (2020).
- [65] N. Hosono and S.-I. Karato, The influence of equation of state on the giant impact simulations, *J. Geophys. Res.: Planets* **127**, e2021JE006971 (2022).
- [66] F. González-Cataldo, F. Soubiran, H. Peterson, and B. Militzer, Path integral monte carlo and density functional molecular dynamics simulations of warm dense MgSiO<sub>3</sub>, *Phys. Rev. B* **101**, 024107 (2020).
- [67] M. Millot, S. Zhang, D. E. Fratanduono, F. Coppari, S. Hamel, B. Militzer, D. Simonova, S. Shcheka, N. Dubrovinskaia, L. Dubrovinsky, and J. H. Eggert, Recreating giants impacts in the laboratory: Shock compression of MgSiO<sub>3</sub> bridgmanite to 14 mbar, *Geophys. Res. Lett.* **47**, e2019GL085476 (2020).
- [68] D. E. Fratanduono, M. Millot, R. G. Kraus, D. K. Spaulding, G. W. Collins, P. M. Celliers, and J. H. Eggert, Thermodynamic properties of MgSiO<sub>3</sub> at super-earth mantle conditions, *Phys. Rev. B* **97**, 214105 (2018).
- [69] C. A. McCoy, S. X. Hu, M. C. Marshall, D. N. Polsin, D. E. Fratanduono, Y. H. Ding, P. M. Celliers, T. R. Boehly, and D. D. Meyerhofer, Measurement of the sound velocity and grüneisen parameter of polystyrene at inertial confinement fusion conditions, *Phys. Rev. B* **102**, 184102 (2020).
- [70] J. Delettrez, R. Epstein, M. C. Richardson, P. A. Jaanimagi, and B. L. Henke, Effect of laser illumination nonuniformity on the analysis of time-resolved x-ray measurements in uv spherical transport experiments, *Phys. Rev. A* **36**, 3926 (1987).
- [71] I. V. Igumenshchev, W. Seka, D. H. Edgell, D. T. Michel, D. H. Froula, V. N. Goncharov, R. S. Craxton, L. Divol, R. Epstein, R. Follett, J. H. Kelly, T. Z. Kosc, A. V. Maximov, R. L. McCrory, D. D. Meyerhofer, P. Michel, J. F. Myatt, T. C. Sangster, A. Shvydky, S. Skupsky *et al.*, Crossed-beam energy transfer in direct-drive implosions, *Phys. Plasmas* **19**, 056314 (2012).
- [72] D. Cao, G. Moses, and J. Delettrez, Improved non-local electron thermal transport model for two-dimensional radiation hydrodynamics simulations, *Phys. Plasmas* **22**, 082308 (2015).
- [73] S. X. Hu, B. Militzer, V. N. Goncharov, and S. Skupsky, Strong Coupling and Degeneracy Effects in Inertial Confinement Fusion Implosions, *Phys. Rev. Lett.* **104**, 235003 (2010).
- [74] S. X. Hu, B. Militzer, V. N. Goncharov, and S. Skupsky, First-principles equation-of-state table of deuterium for inertial confinement fusion applications, *Phys. Rev. B* **84**, 224109 (2011).
- [75] S. X. Hu, L. A. Collins, V. N. Goncharov, T. R. Boehly, R. Epstein, R. L. McCrory, and S. Skupsky, First-principles opacity table of warm dense deuterium for inertial-confinement-fusion applications, *Phys. Rev. E* **90**, 033111 (2014).
- [76] S. X. Hu, L. A. Collins, J. P. Colgan, V. N. Goncharov, and D. P. Kilcrease, Optical properties of highly compressed polystyrene: An *ab initio* study, *Phys. Rev. B* **96**, 144203 (2017).
- [77] J. MacFarlane, I. Golovkin, P. Wang, P. Woodruff, and N. Pereyra, Spect3d a multi-dimensional collisional-radiative code for generating diagnostic signatures based on hydrodynamics and pic simulation output, *High Energy Density Phys.* **3**, 181 (2007).
- [78] See Supplemental Material at <http://link.aps.org/supplemental/10.1103/PhysRevE.106.045207> for the EOS table.
- [79] S. X. Hu, L. A. Collins, T. R. Boehly, Y. H. Ding, P. B. Radha, V. N. Goncharov, V. V. Karasiev, G. W. Collins, S. P. Regan, and E. M. Campbell, A review on *ab initio* studies of static, transport, and optical properties of polystyrene under extreme conditions for inertial confinement fusion applications, *Phys. Plasmas* **25**, 056306 (2018).